

DC Electrical Resistivity and Magnetic Properties of Co Substituted NiCuZn Nano Ferrite

Kanta Jayadev

Andhra University

M. K. Raju

WISTM Engineering College

N MURALI (✉ muraliphdau@gmail.com)

Andhra University <https://orcid.org/0000-0002-8272-2802>

Parajuli D

Andhra University

K. Samatha

Andhra University

Research Article

Keywords: sol-gel auto-combustion process, FTIR spectra, single domain ferrimagnetic particles

Posted Date: February 9th, 2021

DOI: <https://doi.org/10.21203/rs.3.rs-195513/v1>

License:   This work is licensed under a Creative Commons Attribution 4.0 International License.

[Read Full License](#)

DC Electrical resistivity and Magnetic properties of Co substituted NiCuZn nano ferrite

Kanta Jayadev¹, M. K. Raju², N. Murali^{3,*}, D. Parajuli¹, K. Samatha¹

¹Department of Physics, Andhra University, Visakhapatnam

²Department Physics, WISTM Engineering College, Pinagadi, Visakhapatnam

³Department of Physics, Andhra University College of Engineering (A),
Visakhapatnam, India

*Corresponding author: muraliphda@gmail.com

Co substituted $\text{Ni}_{0.3-x}\text{Co}_x\text{Cu}_{25}\text{Zn}_{0.45}\text{Fe}_2\text{O}_4$ ($x = 0, 0.05, 0.1, 0.15$ and 0.2) samples is synthesized using the sol-gel auto-combustion process. X-ray diffraction shows its cubic spinel structure. The lattice constant decreases as the Co content increases. The sizes of the crystallites are in the range of 20.18–26.24 nm. The wavenumbers of tetrahedral and octahedral sites sighted in the FTIR spectra are similar to that of the precursor. The increment on the Co content increases the DC conductivity. The electrical resistivity decrease with increase in the temperature, i.e. it has a negative temperature coefficient with resistance similar to semiconductors. The remnant ratios R obtained from VSM show their isotropic nature forming single domain ferrimagnetic particles. The resultant material is widely significant, as indicated by its result.

Introduction

These spinel nanomaterials or ferrites with cations in their tetrahedral and octahedral sites are used as soft magnetic materials in everyday life [1-3]. On changing their internal with doping can make them applicable in more advanced devices. Most of the spinel ferrite materials have $\text{M}^{2+}\text{Fe}_2^{3+}\text{O}_4^{2-}$ the type of structure, where, M is Transitional Metal Cation. M is on the tetrahedral site and Fe on the octahedral site of the spinel. This soft magnetic ferrite's high resistivity and low power loss made them be used in multilayered chip inductors, microwave absorption materials, information storage system, transformer core, computer circuitry and electronic communication. Among them, Ni-Zn ferrite is one that is highly stable at a higher frequency. Ni-Cu-Zn ferrites are used in Multilayer Chip Inductors (MLCI) and Surface Mounting Devices (SMDs). As a result, they are utilized in cellular phones, video cameras, notebook computers, personal wireless communication systems, etc. their properties can be changed by varying the concentration of Co^{2+} and

found to be more applicable in inductive devices like transformers. [4-7]. The ferrites prepared at low temperature are used in multilayer power inductors and transformers.

In this work, Co substituted $\text{Ni}_{0.3-x}\text{Co}_x\text{Cu}_{25}\text{Zn}_{0.45}\text{Fe}_2\text{O}_4$ ($x = 0, 0.05, 0.1, 0.15$ and 0.2) ferrites are prepared by sol-gel auto combustion method, and their different properties are studied using XRD, FESEM, FTIR, DC resistivity, VSM etc.

EXPERIMENTAL TECHNIQUES

Co Substituted NiCuZn nanoparticles are prepared by the sol-gel auto-combustion method. 99.99% pure Nickel nitrate, Cobalt nitrate, Copper nitrate, Zinc nitrate, Iron nitrate and citric acid monohydrate with the molecular formula $\text{Ni}(\text{NO}_3)_2 \cdot 6\text{H}_2\text{O}$, $\text{Co}(\text{NO}_3)_2 \cdot 6\text{H}_2\text{O}$, $\text{Zn}(\text{NO}_3)_2 \cdot 6\text{H}_2\text{O}$, $\text{Cu}(\text{NO}_3)_3 \cdot \text{H}_2\text{O}$, $\text{Fe}(\text{NO}_3)_3 \cdot 9\text{H}_2\text{O}$ and $\text{C}_6\text{H}_8\text{O}_7 \cdot \text{H}_2\text{O}$ respectively, as the starting materials. They are mixed in such a ratio that Co substituted $\text{Ni}_{0.3-x}\text{Co}_x\text{Cu}_{25}\text{Zn}_{0.45}\text{Fe}_2\text{O}_4$ ($x = 0, 0.05, 0.1, 0.15$ and 0.2) samples are prepared. These metal nitrates and citric acid were mixed in molar ratio 1:1 and were dissolved in the distilled water to get a clear solution. The solution was made neutral by adding liquid ammonia. The solution was then stirred in magnetic stirrer maintained at 100°C for 4 h, decanted and dried at normal temperature for 12 h. The flakes thus obtained were combusted and converted into a powder. The powder was sintered in a muffle furnace at 800°C for 4 h at $5^\circ/\text{min}$.

We used Rigaku X-ray diffractometer (Rigaku Miniflex II) incorporated with $\text{CuK}\alpha$ radiation of wavelength = 1.5406 \AA for the structural property, TESCAN, MIRA II LMH FESEM with attached Inca Oxford EDX for textural and compositional images, FT-IR analysis for the detection of functional group, EZ VSM model for the magnetic at room temperature. Few drops of polyvinyl alcohol were mixed with the powder for shaping them into disc-like pallets after pressing them in a die under the hydraulic press of 5 tons. The pallets were then made as an electrode by sintering them in 800°C in a muffle furnace and polishing their flat sides with gold. Their conductivity was checked by the two-probe DC resistivity method.

3. RESULTS AND DISCUSSIONS

3.1 XRD Studies

The XRD plots of different Co substituted $\text{Ni}_{0.3-x}\text{Co}_x\text{Cu}_{25}\text{Zn}_{0.45}\text{Fe}_2\text{O}_4$ ($x = 0, 0.05, 0.1, 0.15$ and 0.2) samples are shown in Figure 1. The structure of the sample is found to be cubic spinel structure according to the JCPDS card No.48- 0489. The lattice constant ‘a’ is determined with the following relation [8].

$$a = d_{hkl} \sqrt{h^2 + k^2 + l^2}$$

where d_{hkl} is interplaner spacing for given hkl planes and is calculated by Bragg’s law. The plot of intensity against the diffracting angle (2θ) for different concentration of Co, $x = 0, 0.05, 0.1, 0.15$ and 0.2 in $\text{Ni}_{0.3-x}\text{Co}_x\text{Cu}_{25}\text{Zn}_{0.45}\text{Fe}_2\text{O}_4$ ferrite nanoparticles (NPs) are shown in Figure 2. The highest intensity (311) peak indicates the crystallites appropriate orientation to measure its degree of crystalline nature to find the average crystallite size of all samples [9]. Debye-Scherer’s formula gives the average size of the crystallite size [10].

$$D_{311} = \frac{0.9\lambda}{\beta \cos\theta}$$

where, D_{311} , λ , β and θ are volume-averaged crystallite size, the wavelength of X-ray (1.5406\AA), full width at half maximum of (311) peak and diffraction angle respectively.

The crystallite size, lattice parameters and cell volume of the composition Co substituted $\text{Ni}_{0.3-x}\text{Co}_x\text{Cu}_{25}\text{Zn}_{0.45}\text{Fe}_2\text{O}_4$ ($x = 0, 0.05, 0.1, 0.15$ and 0.2) is listed in Table 1. The increasing-decreasing pattern of crystallite size is due to the lattice strain produced in the synthesis process as the number of disorder decreases, the size of the crystal increases. In contrast, the lattice parameter decreases with the Co^{2+} ions concentration. This is due to the greater ionic radius of Ni^{2+} ions (0.74\AA) [12] as compared Co^{2+} (0.72\AA) [13] thereby expanding the unit cell or decreasing lattice constant [14] as shown in figure 3. The obtained value of the lattice parameter of the base ($x = 0$) sample is 8.3956\AA . It is well-matched with the value reported in literature 8.3963\AA [31], 8.3923\AA [32] and 8.392\AA [33]. The lattice compression may also be due to the partial oxidation of Ni^{2+} to Ni^{3+} , Co^{2+} to Co^{3+} . The zinc loss and gain are usually credited to the surface, forming a common boundary structure between surfaces with a more volume fraction. The variation of lattice constant is more significant in a smaller size of the nanoparticle. From Scherer’s formula, the diffraction peak width (β) is inversely proportional to the crystallite size. The increase in the lattice parameter expands the volume of the unit cell accordingly. Sintering

decreases the lattice defects and involved strain but facilitates the crystals' coalition increasing in particle size.

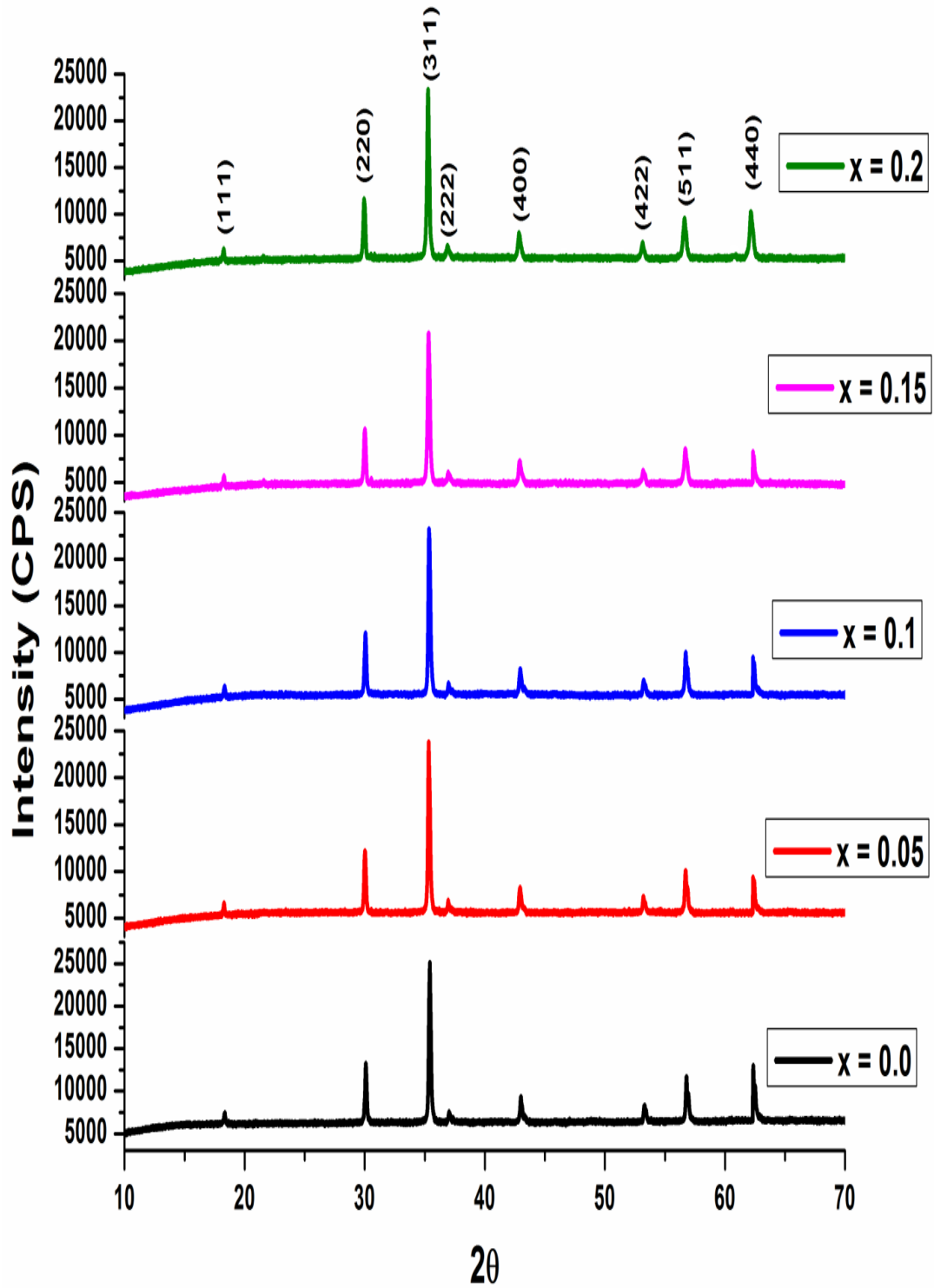


Figure 1: X-ray diffraction patterns of Co substituted NiCuZn ferrite

TABLE 1: Lattice parameters of Co substituted NiCuZn ferrite

Concentration (x)	a (Å)	Crystallite (nm)	Space Group
0.0	8.3956	20.18	$Fd-3m$
0.05	8.3921	21.51	$Fd-3m$
0.1	8.3908	26.24	$Fd-3m$
0.15	8.3871	24.57	$Fd-3m$
0.2	8.3799	25.84	$Fd-3m$

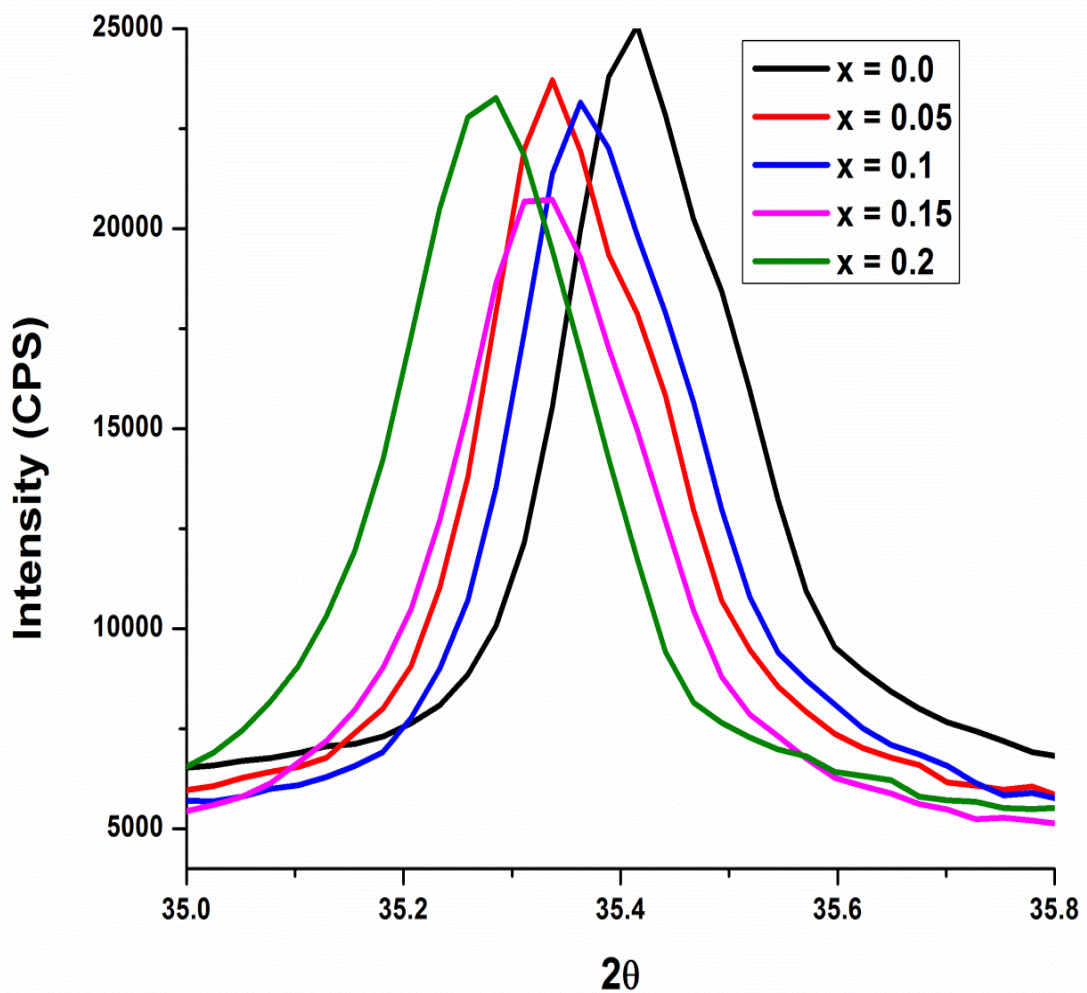


Figure 2: XRD patterns of Intensity vs Angle Co substituted NiCuZn ferrite

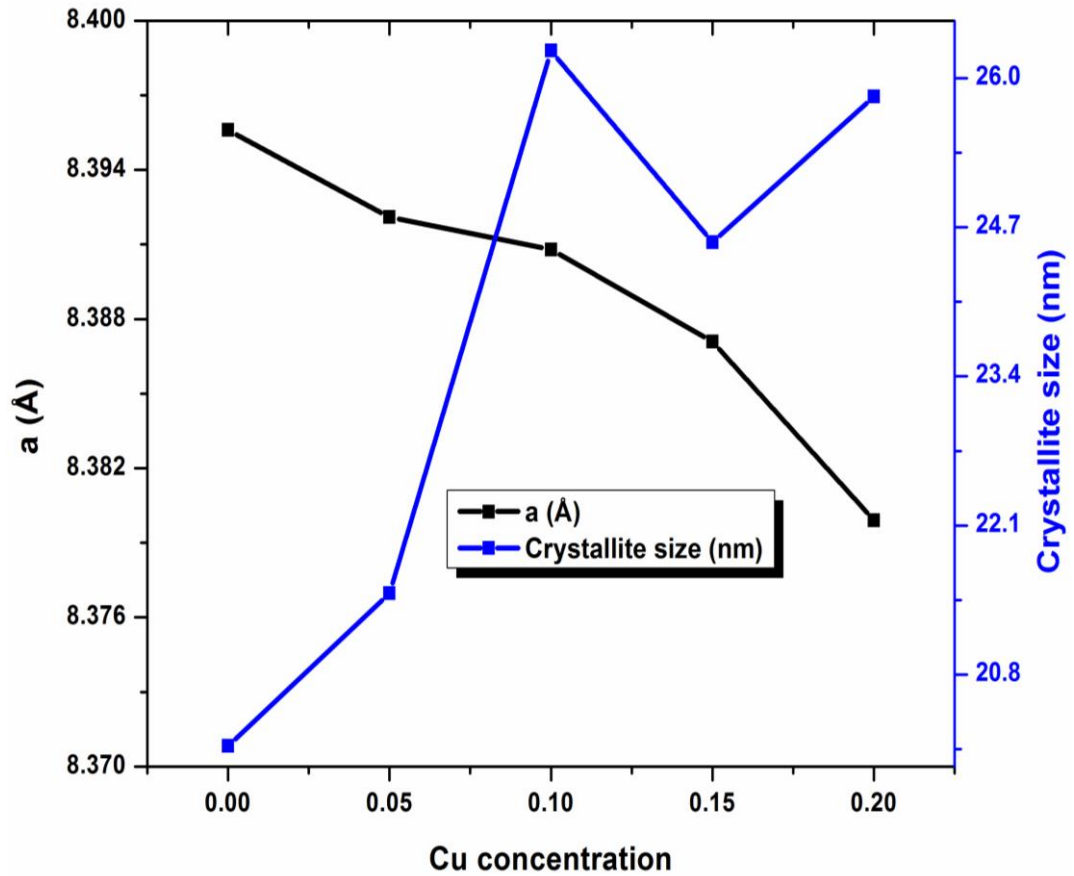


Figure 3: Variation of lattice constant and crystallite size of Co substituted NiCuZn ferrite

3.2 Field-Effect Scanning Electron Microscope (FESEM) studies

The microstructure images like grain size, pores, inclusions, grain boundaries, particle size, homogeneity, defects etc. can be obtained with the help of Electron microscope. The smaller grain size with low porosity controls unnecessary spin-wave production, which is essential for microwave devices. Similarly, the large grain size supports the mobility of the domain wall, resulting in high permeability with low coercive value. Also, the eddy current losses is checked by the grain boundaries acting as current barriers. The FESEM images from Figure 4(a) to (e) show that the Co substituted $\text{Ni}_{0.3-x}\text{Co}_x\text{Cu}_{25}\text{Zn}_{0.45}\text{Fe}_2\text{O}_4$ ($x = 0, 0.05, 0.1, 0.15$ and 0.2) sample average size of the grain ranges from 100 to 150 nm. The grains sizes are nearly equal [15].

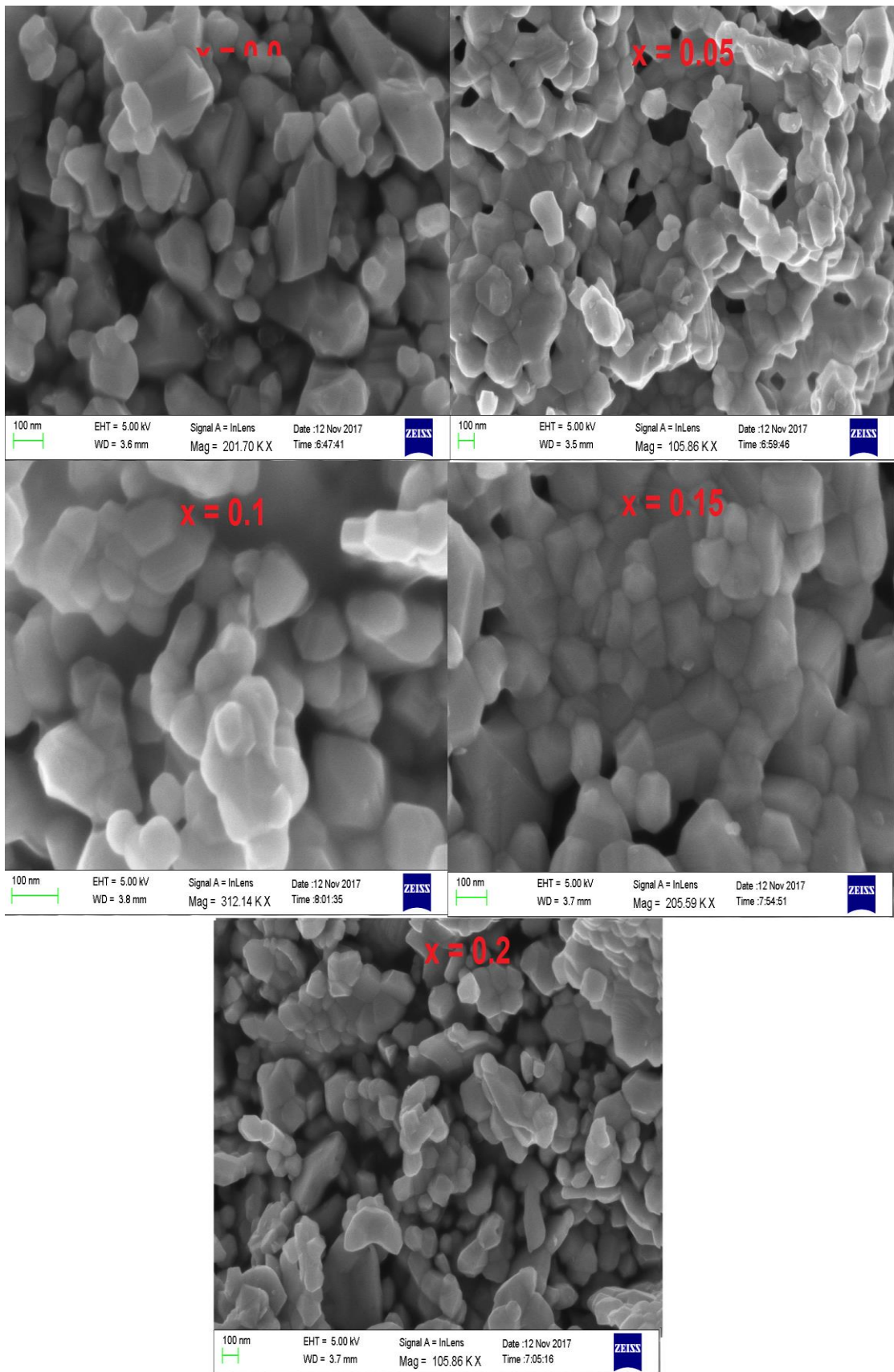


Figure 4: FESEM images for of Co substituted NiCuZn ferrite

3.3 Fourier Transformed Infrared (FTIR) Spectroscopy studies

The FTIR spectroscopy helps determine the different functional groups for their wavenumbers or how the absorption occurs. The FTIR spectra of Co substituted $\text{Ni}_{0.3-x}\text{Co}_x\text{Cu}_{25}\text{Zn}_{0.45}\text{Fe}_2\text{O}_4$ ($x = 0, 0.05, 0.1, 0.15$ and 0.2) sample within the range of $400\text{-}4000\text{ cm}^{-1}$ are as shown in figure 6. The spinel or inverse spinel ferrite can show four IR active regions or high intensity or non-zero dipole moment regions in the vibrational spectra. First, three of them are the resultant of octahedral and tetrahedral compounds, and the fourth is due to the lattice vibration of the tetrahedral cation. The two absorption bands at wavenumbers 580.4 to 599.3 cm^{-1} and 402.1 to 408.2 cm^{-1} seen as two depressions in figure 6 and values listed in Table 2 are the two respective characteristics bands of each spinel ferrite. The FT-IR spectra exhibit prominent bands in the range of wave numbers $3423\text{--}3442\text{ cm}^{-1}$, $2350\text{--}2385\text{ cm}^{-1}$ and $1633\text{--}1637\text{ cm}^{-1}$ attributed to the tensional stretching modes and H-O-H bending vibration of the free or absorbed water molecules [21]. The bond length between Fe^{3+} and O^{2-} is varied for the sample composition, resulting in the deviation in the peak position of ν_1 and ν_2 towards high-frequency region [16].

Table 2: Absorption bands of Co substituted NiCuZn ferrite

Concentration (x)	Tetrahedral $\nu_1(\text{cm}^{-1})$	Octahedral $\nu_2(\text{cm}^{-1})$
0.0	402.1	580.4
0.05	403.2	583.2
0.1	405.6	586.0
0.15	408.2	590.2
0.2	406.1	599.3

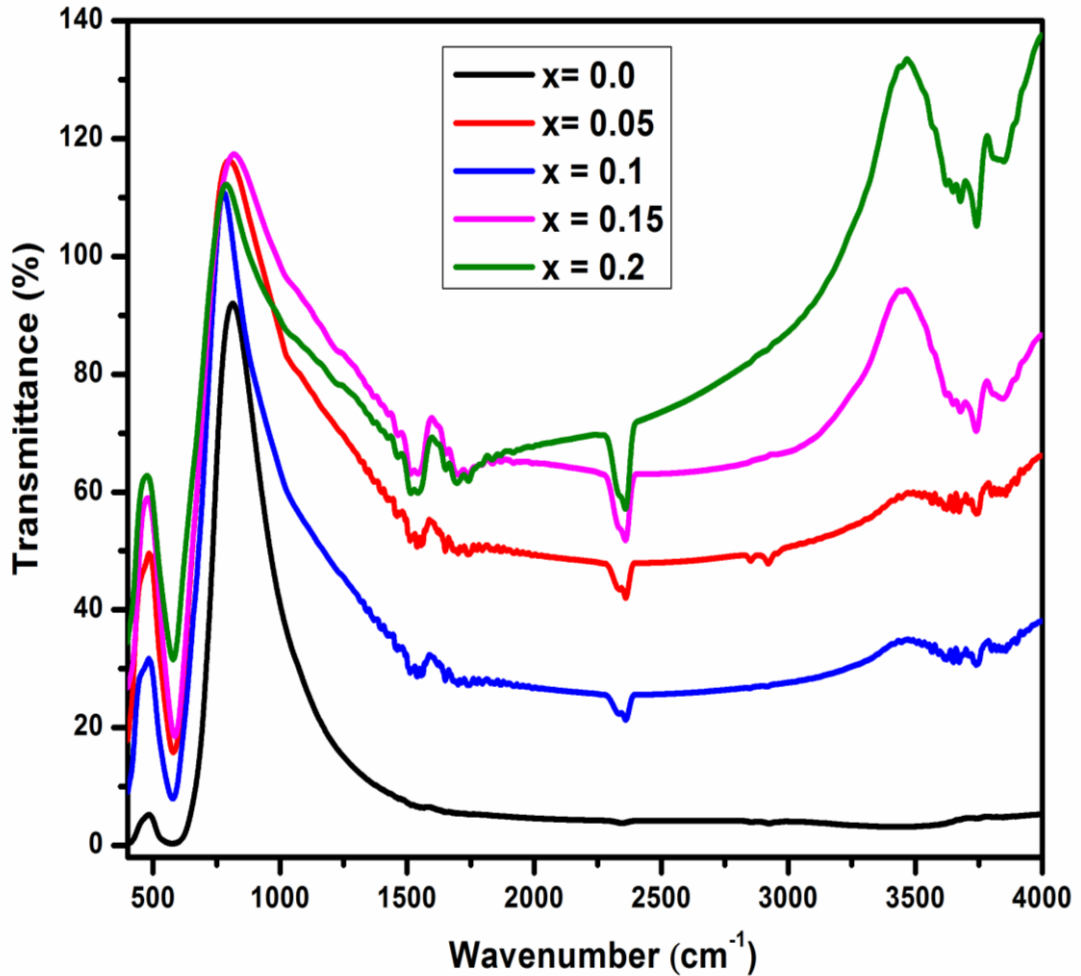


Figure 6: Infrared spectra of Co substituted NiCuZn ferrite

3.4 Magnetic properties

Ferrites have antimagnetic moments with unequal magnitudes. As a result, they have a large value of spontaneous magnetization. The exchange integral, depending on interatomic distance, is negative for ferrite. This indirect exchange interaction through oxygen ions limits the easy flow of electron. So, ferrites have high resistivity [17].

The magnetic properties like saturation permeability, coercivity, susceptibility, Curie temperature etc. of ferrites depend on the concentration of metal ions on both the octahedral and tetrahedral sites. The hysteresis loop shapes, resistivity, ac conductivity, and dielectric constant depend on the ferrite structure. So, these properties are more sensitive to the structure. These properties can be changed by adding external magnetic or non-magnetic metal ions. The hysteresis curves of our

respective samples are as shown in figure 7. They give the values of coercivity (H_c), saturation magnetization (M_s) etc. that are important for their magnetic properties. The values of M_s and H_c are listed in Table 3 [18].

From table 3, M_s increases up to ($x \leq 0.1$) and then starts decreasing with Co^{2+} concentration. This is due to the distribution of cations and exchange interaction. On adding Co substituted $\text{Ni}_{0.3-x}\text{Co}_x\text{Cu}_{25}\text{Zn}_{0.45}\text{Fe}_2\text{O}_4$ ($x = 0, 0.05, 0.1, 0.15$ and 0.2), they exchange few magnetic ions Fe^{3+} and Ni^{2+} in B- site increases AB interaction that interrupts the antiparallel spin at B site resulting from the increase in total magnetization [19]. A similar phenomenon occurs on the A site. The A-B and B-A interaction dominate the A-A and B-B interaction according to as Weiss Molecular field theory resulting in the hysteresis loop [20-21].

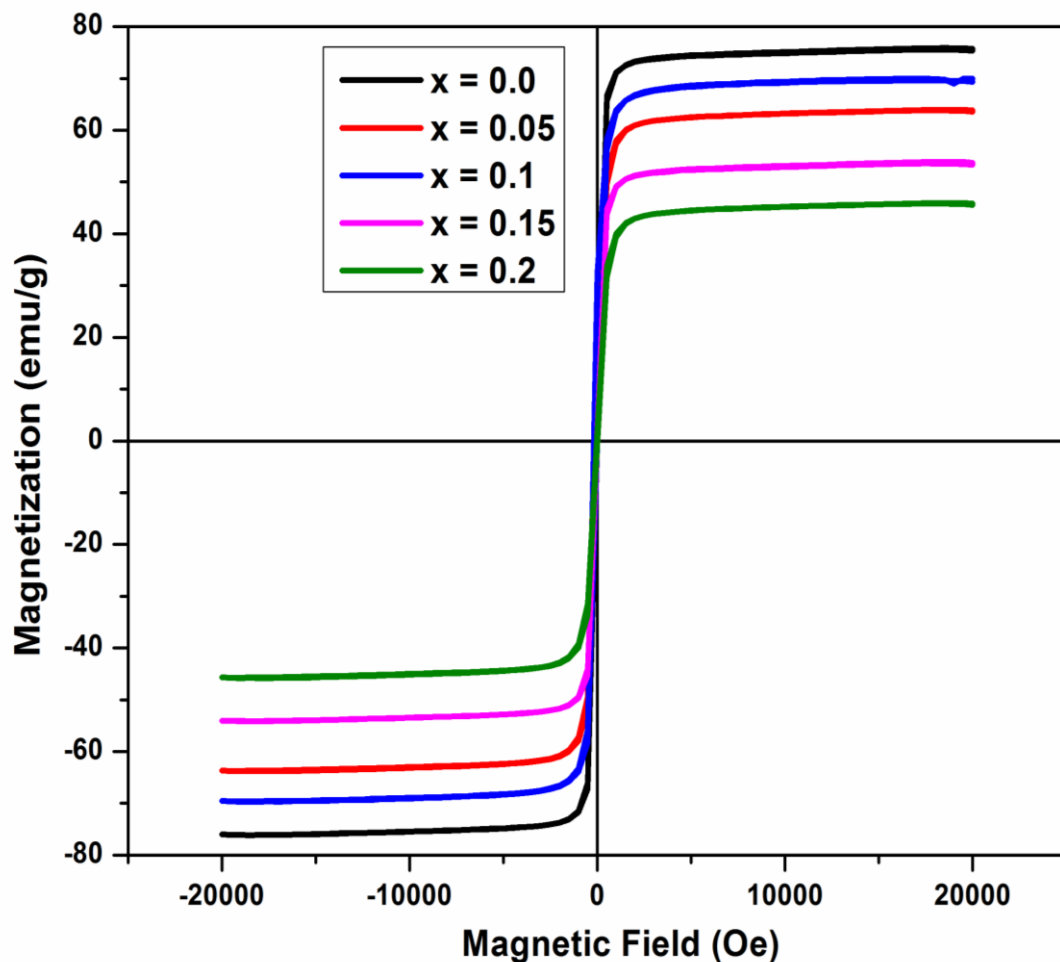


Figure 7: Hysteresis curve of Co substituted NiCuZn ferrite

Table 3: Ms and Hc of Co substituted NiCuZn ferrite

Concentration (x)	Ms (emu/g)	Hc (Oe)
0.0	73.26	45.36
0.05	63.61	40.62
0.1	69.39	43.45
0.15	56.05	65.26
0.2	46.32	51.48

3.5 DC Electrical Resistivity

The DC resistivities of Co substituted $\text{Ni}_{0.3-x}\text{Co}_x\text{Cu}_{2.5}\text{Zn}_{0.45}\text{Fe}_2\text{O}_4$ ($x = 0, 0.05, 0.1, 0.15$ and 0.2) ferrites nanoparticles initially decreases rapidly, then steadily and then continue with the further increase in Co concentration. The plot of DC resistivity vs temperature for the Co substituted NiCuZn is shown in figure 8. A graph between $\log \rho$ and $1000/T$ is a straight line. It shows that the resistivity decreases with increase in temperature showing semiconducting behaviour. The slope of the line gives the activation energies of the ferrite samples. The dc resistivity data are used in Arrhenius to find the activation energy of the thermally activated hopping of charge carriers [22].

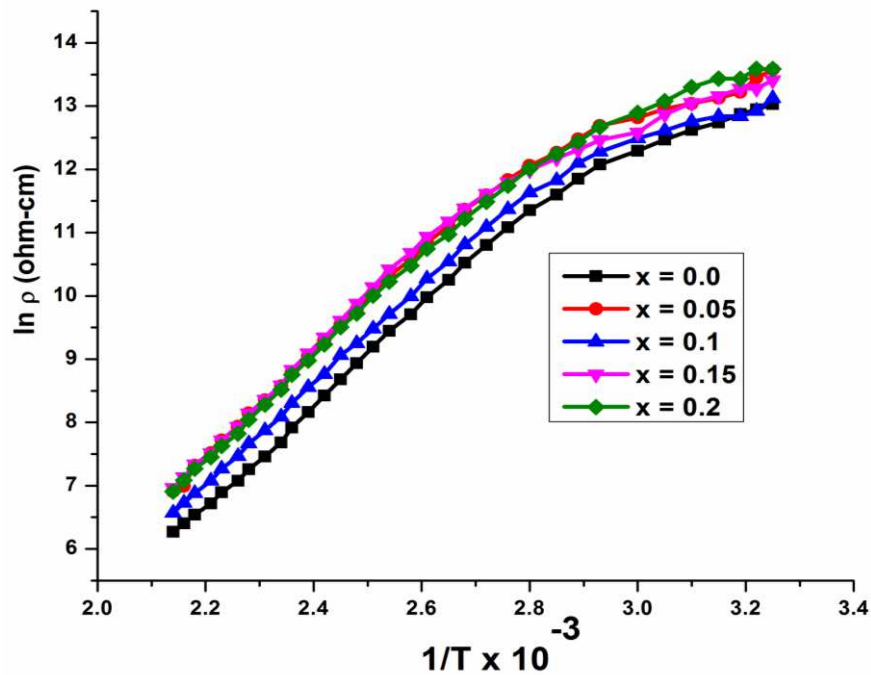


Figure 8: Temperature dependence of DC resistivity of Co substituted NiCuZn ferrite

The Arrhenius relation is,

$$\rho = \rho_0 e^{-\left(\frac{\Delta E}{KT}\right)}$$

where ρ is the dc electrical resistivity at temperature T , ρ_0 is the pre-exponential factor ΔE is the activation energy, K is the Boltzmann constant and T is the absolute temperature. The calculated values of activation energies of the Co substituted $\text{Ni}_{0.3-x}\text{Co}_x\text{Cu}_{25}\text{Zn}_{0.45}\text{Fe}_2\text{O}_4$ ($x = 0, 0.05, 0.1, 0.15$ and 0.2) ferrite nanoparticles ferrite samples are shown in Figure 9. Verwey and de Boer hopping mechanism helps to interpret the resistivity variation for the Cu doped Ni-Zn ferrite nanoparticles. Electron hopping occurs between ions of the same element located at different valance states and the two sites. During sintering of the ferrites, the divalent and trivalent iron ions can be produced and exist in octahedral sites that help in electrical conduction through $\text{Fe}^{2+} \leftrightarrow \text{Fe}^{3+}$ hopping mechanism. If the ferrite's sintering temperature is higher, more Fe^{2+} ions are produced, thereby accelerating the hopping process. The hopping process is also possible in $\text{Ni}^{2+} \leftrightarrow \text{Ni}^{3+}$ and $\text{Co}^{3+} \leftrightarrow \text{Co}^{2+}$ existing together in a system [23].

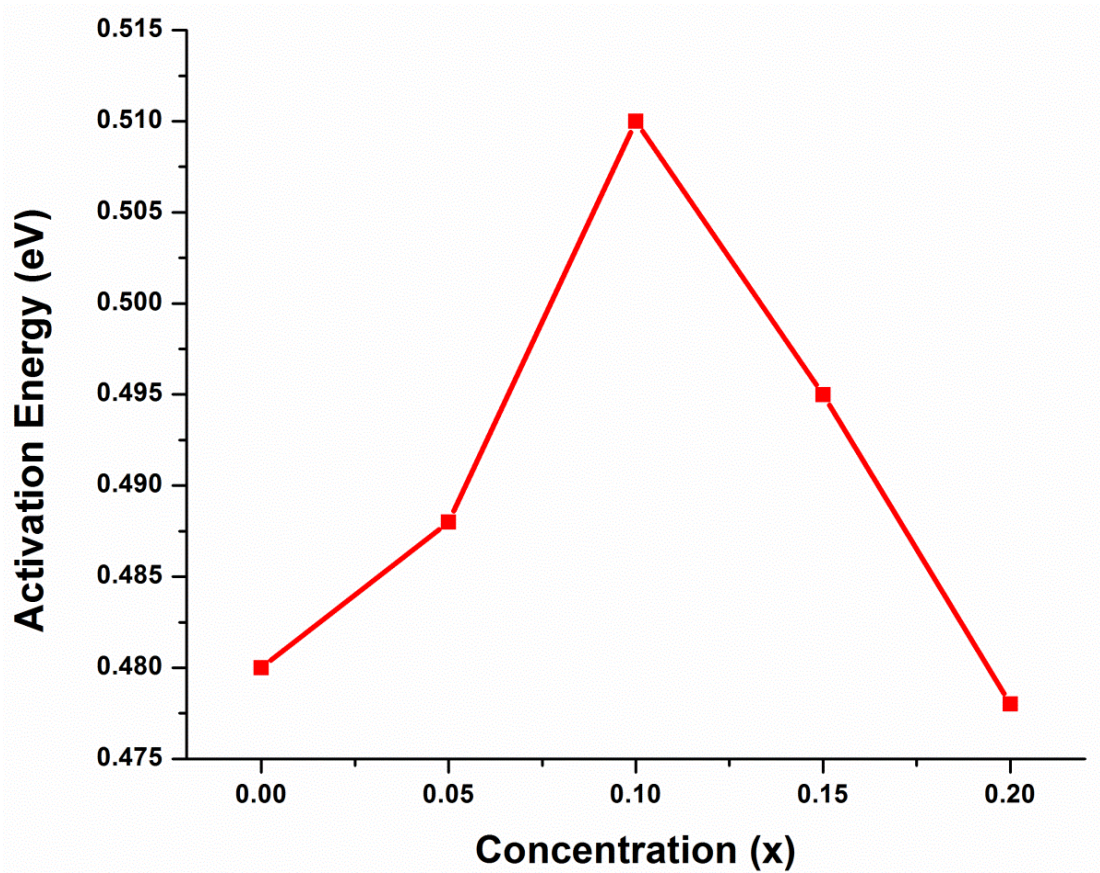


Figure 9: Activation energies of the Co substituted NiCuZn ferrite

About the above calculation as in figure 8, the activation energies are found to be in the order of 0.42 to 0.51 eV which is for the $\text{Fe}^{2+} \leftrightarrow \text{Fe}^{3+}$ electron hopping mechanism. It indicates that the major conduction mechanism is $\text{Fe}^{2+} \leftrightarrow \text{Fe}^{3+}$ process. Besides, the conduction processes such as $\text{Fe}^{2+} + \text{Zn}^{3+} \leftrightarrow \text{Fe}^{3+} + \text{Zn}^{2+}$ ions require relatively more energy for electron hopping so that the energy required could be slightly more than 0.42 eV. The temperature-dependent resistivity and associated activation energies indicate the compositional dependence of resistivity [24].

4. CONCLUSIONS

Sol-gel auto-combustion method is utilized to fabricate nanocrystalline Co substituted $\text{Ni}_{0.3-x}\text{Co}_x\text{Cu}_{25}\text{Zn}_{0.45}\text{Fe}_2\text{O}_4$ ($x = 0, 0.05, 0.1, 0.15$ and 0.2) ferrite NPs. The structure of the ferrite shown by the X-ray diffraction is single phase cubic spinel. The increasing-decreasing pattern of crystallite size is due to the lattice strain produced in the process of synthesis. In comparison, the lattice parameter decreases with the Co^{2+} ions concentration. This is due to the larger ionic radius of Co^{2+} (0.73 \AA) as compared Ni^{2+} (0.74 \AA), thereby expanding the unit cell or increasing lattice constant. Sintering decreases the lattice defects and involved strain but facilitates the crystals' coalition increasing in particle size. FESEM reveals microstructural growth along with heat action. The FTIR spectrum exhibits a prominent attribute of ferrite microstructure along with major impact of the mixture of ingredients. The magnetic measurements show that magnetization reduces and coercivity enhances as the composition $x = 0.1$. DC resistivity is decreasing with an increase in Co content due to its highly conducting property. The electrical resistivity decrease with increase in the temperature, i.e. it has a negative temperature coefficient with resistance similar to semiconductors. The temperature-dependent resistivity and associated activation energies indicate the compositional dependence of resistivity.

REFERENCES

- [1] Yu S, Wu G, Gu X, Wang J, Wang Y, Gao H, et al. *Colloids Surf*, 103 (2013) 15–22.
- [2] Tejabhram Y, Pradeep R, Helen AT, Gopalakrishnan C, Ramasamy C. *Mater Res Bull* 2014;60:778–82.
- [3] Jha DK, Shameem M, Patel AB, Kostka A, Schneider P, Deb AEP. *Mater Lett* 2013;95:186–9.
- [4] Kenouche S, Larionova J, Bezzi N, Guari Y, Bertin N, Zanca M, et al. *Powder Technol* 2014;255:60–5.
- [5] A. Ramakrishna, N. Murali, Tulu Wegayehu Mammo, K. Samatha, V. Veeraiah, *Phys. B: Condens. Matter* 534 (2018)134-140.
- [6] Min Ji Hyun, Woo Mi-Kyung, Yoon Ha Young, Jang Jin Woo, Wu Jun Hua, Lim Chae-Seung, et al. *Anal Biochem* 2014;447:114–8.
- [7] Drmota A, Koselj J, Drofenik M, Znidarsic A. *J Magn Magn Mater* 2012;324:1225–9.
- [8] B.D. Cullity, (1956), *Elements of X-ray diffraction*, Addison Wesley Publication reading, M.A.
- [9] Costa ACFM, Leite AMD, Ferreira HS, Kiminami RHGA, Cavac S, Gama L. *J Eur Ceram Soc* 2008;28:2033–7.
- [10] C. Nlebedim, K.W. Dennis, R.W. McCallum, D.C. Jiles, *J. Appl. Phys.* 115 (2014) 17A519.
- [11] James V, Rao PP, Sameera S, Divya S. *Ceram Int* 2014;40(Issue 1 Part B):2229–35.
- [12] Netto CGCM, Toma HE, Andrade LH. *J Mol Catal B Enzym* 2013;85–86:71–92.
- [13] Guo F, Fang Z, Xu CC, Smith Jr RL. *Prog Energy Combust Sci*, Oxford, Inglaterra, GB 2012;38 (5):672–90.
- [14] Jing H, Wang X, Liu Y, Wang A. *Chin J Catal* 2015;36(2):244–51.
- [15] Akhtar MN, Khan MA, Ahmad M, Nazir MS, Imran M, Ali A, et al. *J Magn Magn Mater* 2017;421:260–8.
- [16] Ambursa MM, Ali TH, Lee HV, Sudarsanam P, Bhargava SK, Hamid SBA. *Fuel* 2016;180:767–76.
- [17] Li Y, Zhang C, Liu Y, Tang S, Chen G, Zhang R, et al. *Fuel* 2017;189:23–31.
- [18] Jain SR, Adiga KC, Verneker VP. *Combust Flame* 1981;40:71–9.

- [19] Klung H, Alexander L. New York: Wiley; 1962.
- [20] N. Murali, S. Margarete, G.P. Kumar, B. Sailaja, S.Y. Mulushoa, P. Himakar, B. K. Babu, V. Veeraiah, *Phys. B Condens. Matter*, 522 (2017) 1-6
- [21] Reed JS. New York: John Wiley & Sons; 1996.
- [22] Kumar S, Kumar P, Singh V, Kumar Mandal U, Kumar Kotnala R. *J Magn Magn Mater* 2015;379:50–7.
- [23] Andreev VG, Menshova SB, Klimov AN, Vergazov RM. *J Magn Magn Mater* 2015;393:569–73.
- [24] Bato0 KM, Ansari MS. *Nanoscale Res Lett* 2012;7(1):1–14.

Figures

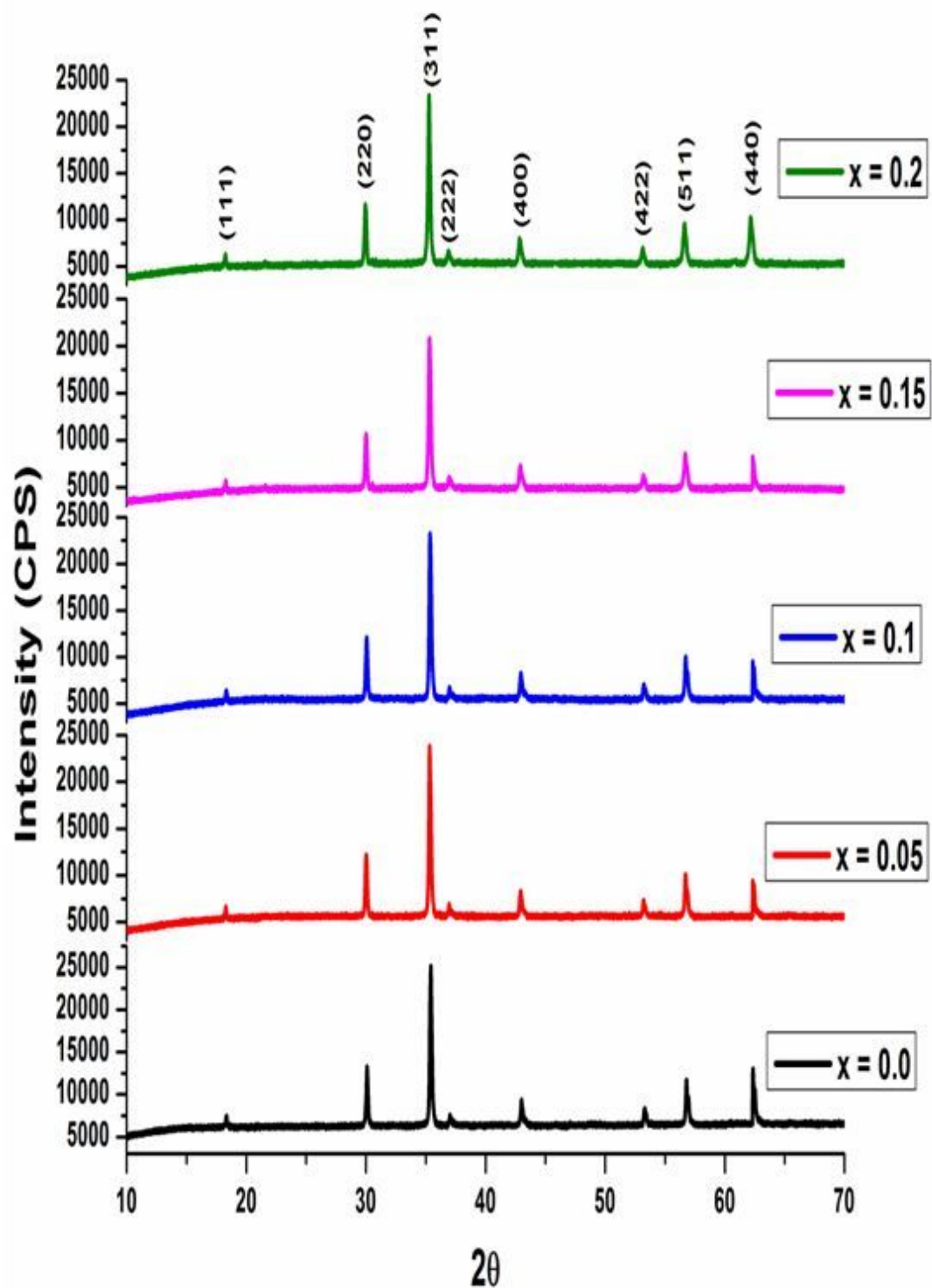


Figure 1

X-ray diffraction patterns of Co substituted NiCuZn ferrite

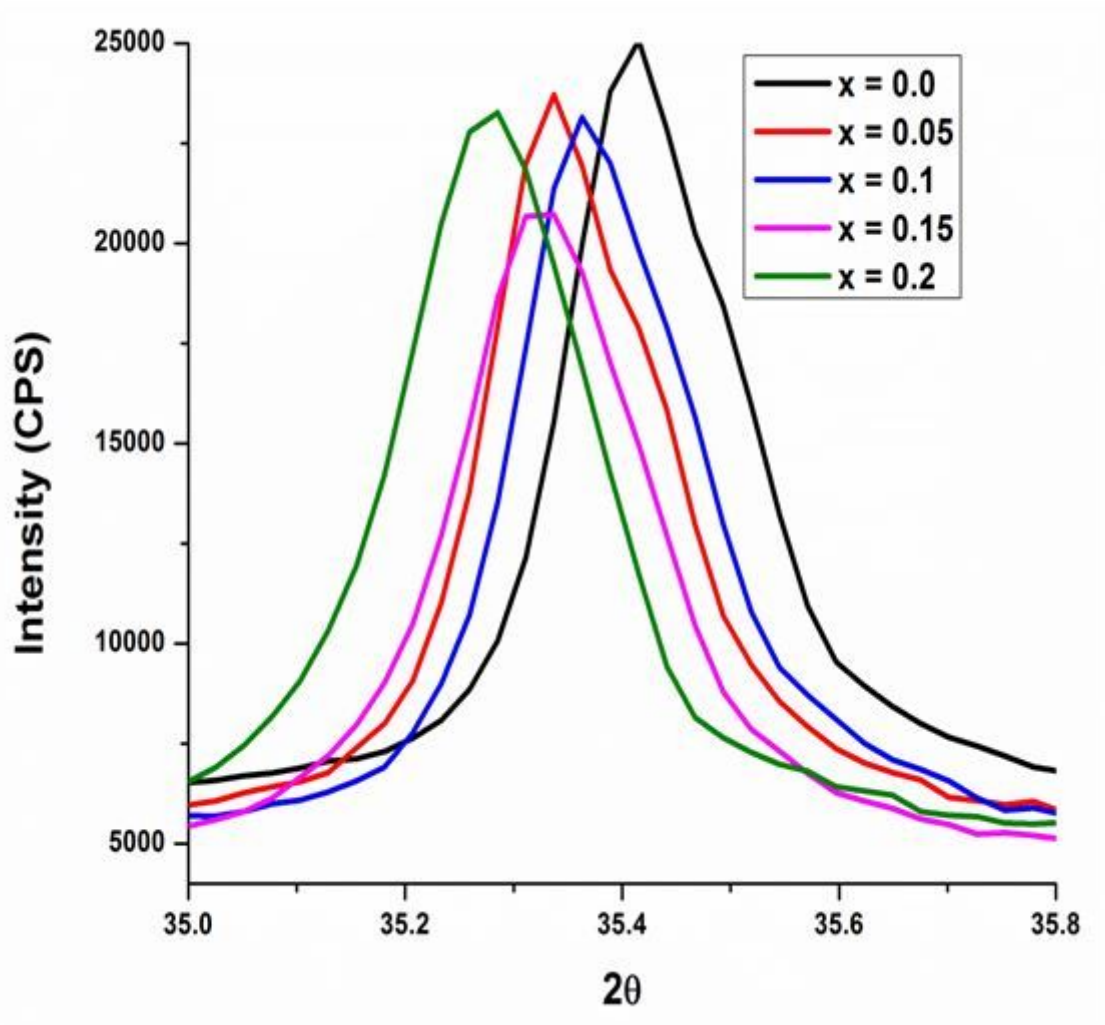


Figure 2

XRD patterns of Intensity vs Angle Co substituted NiCuZn ferrite

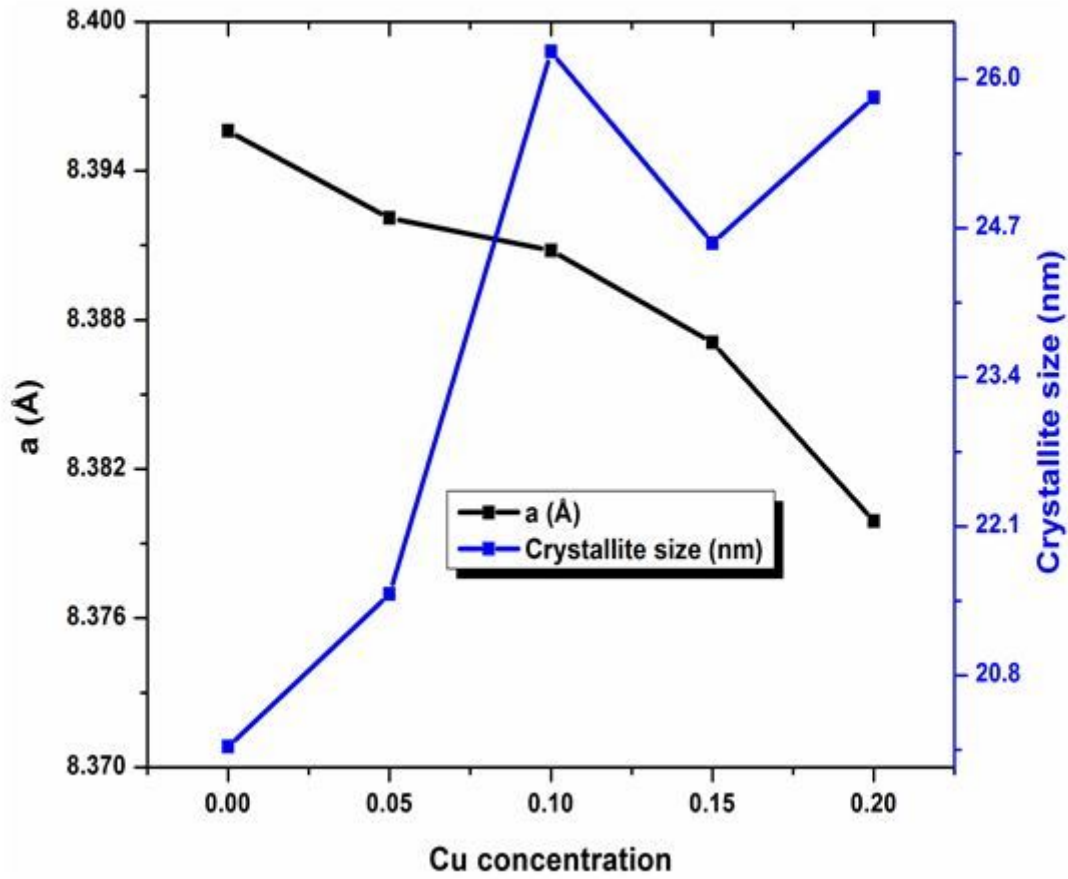


Figure 3

Variation of lattice constant and crystallite size of Co substituted NiCuZn ferrite

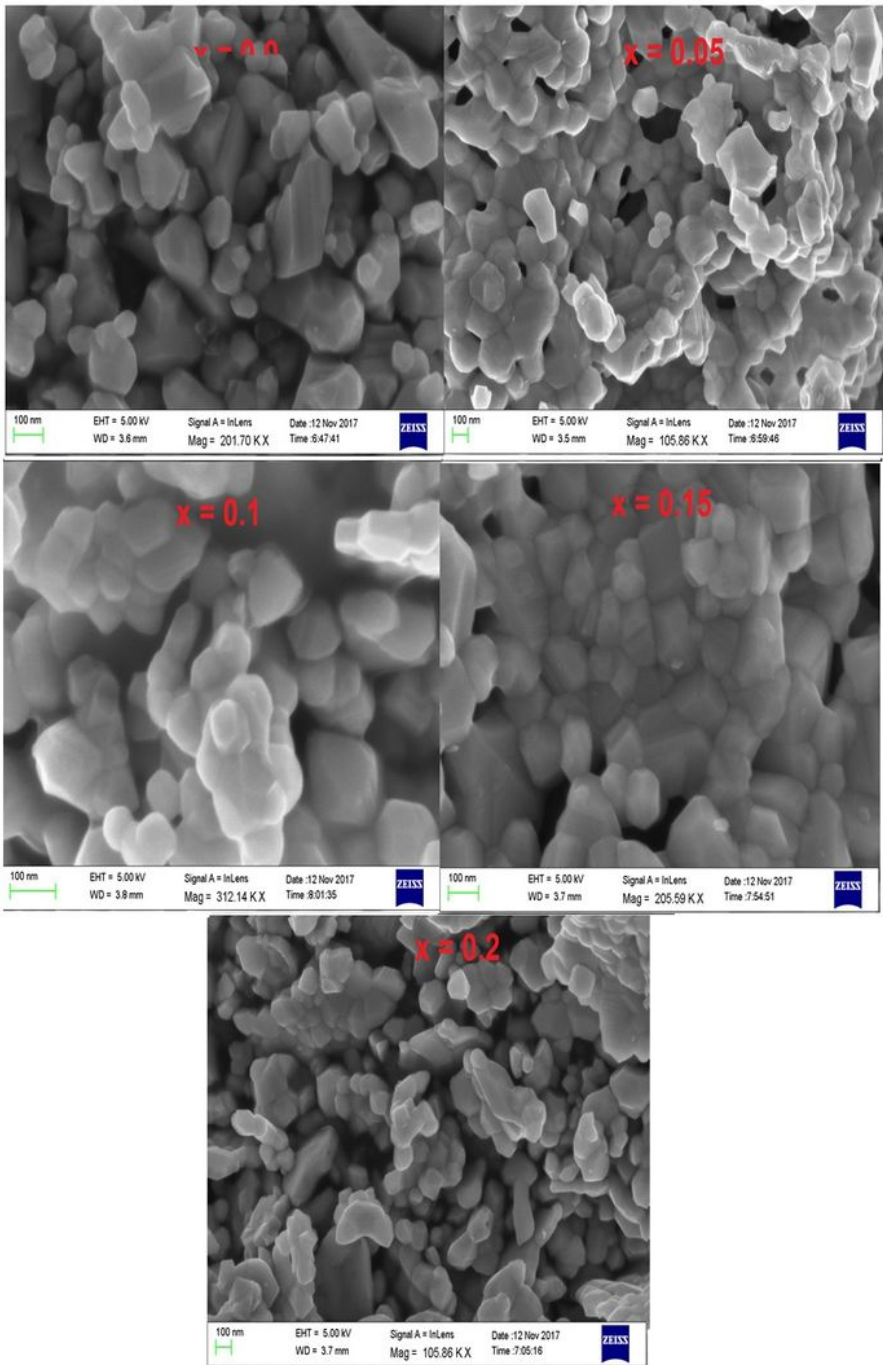


Figure 4

FESEM images for of Co substituted NiCuZn ferrite

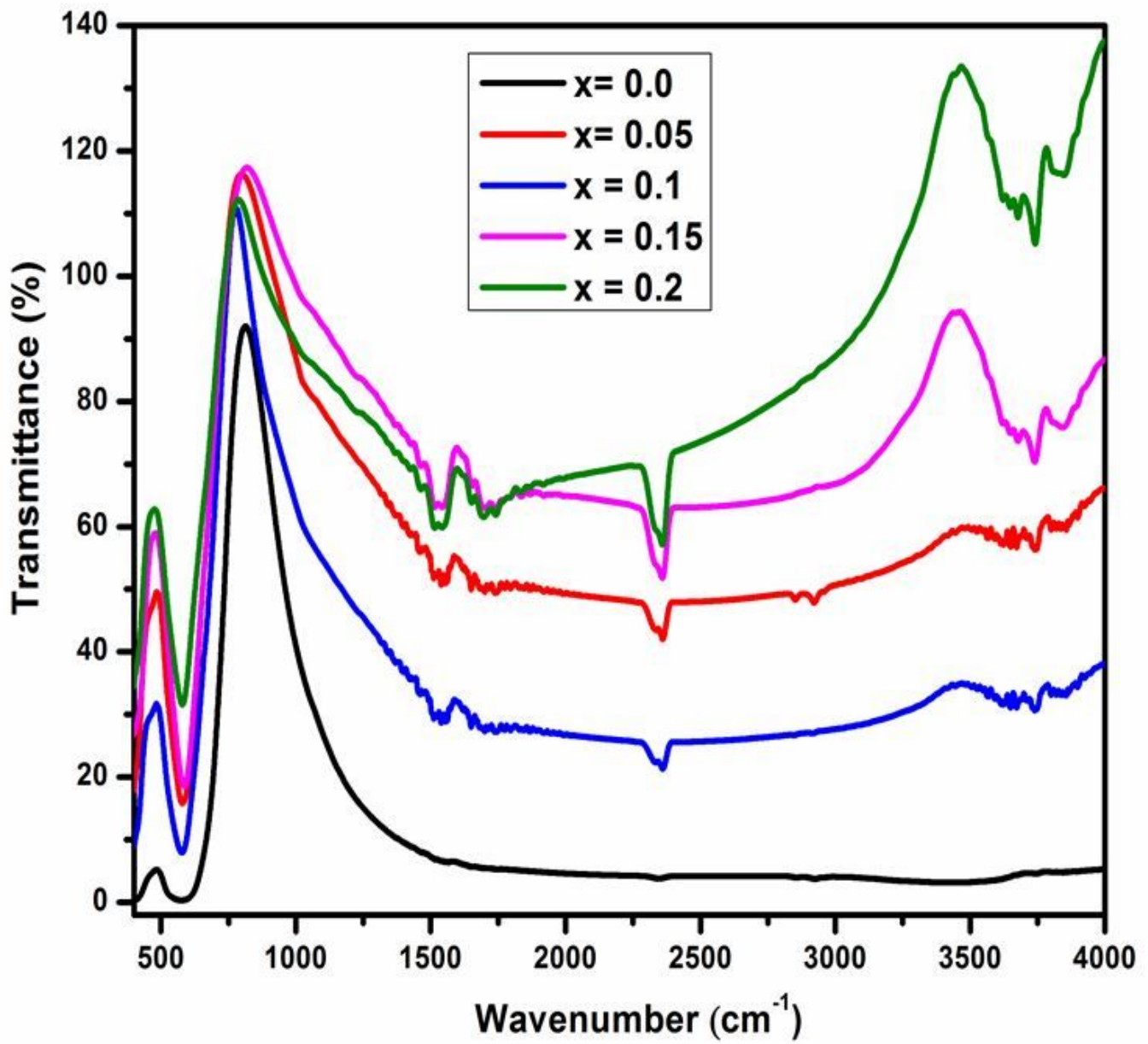


Figure 5

Infrared spectra of Co substituted NiCuZn ferrite

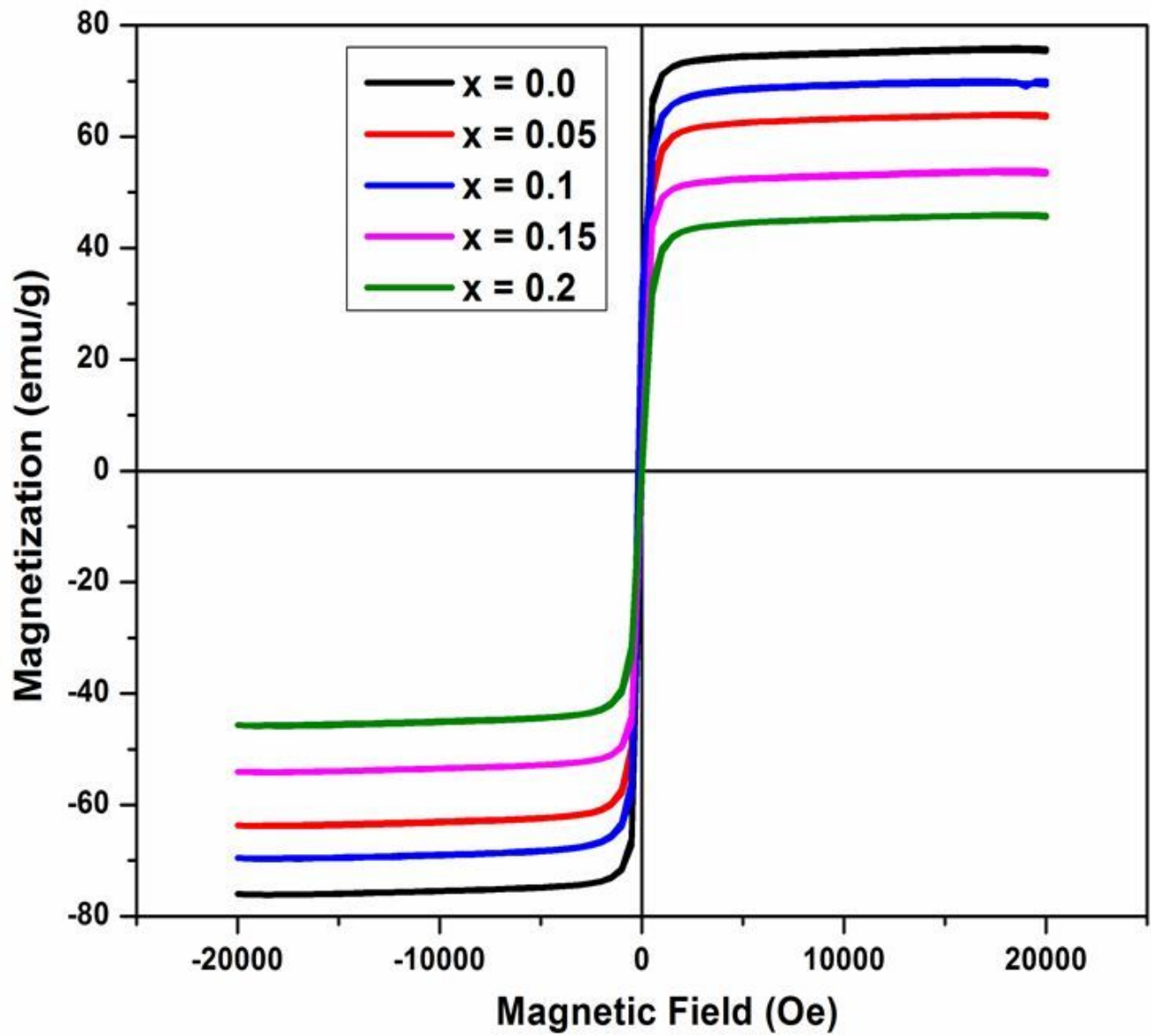


Figure 6

Hysteresis curve of Co substituted NiCuZn ferrite

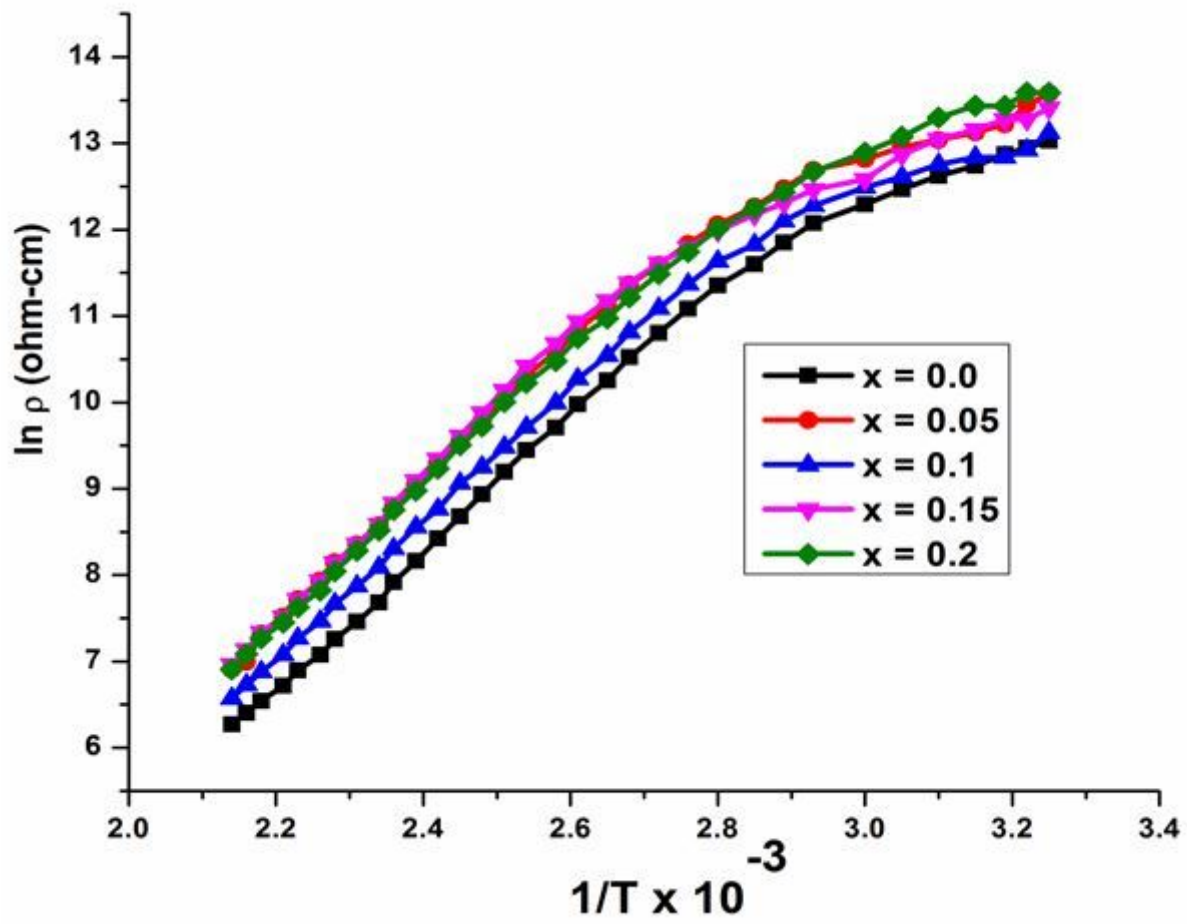


Figure 7

Temperature dependence of DC resistivity of Co substituted NiCuZn ferrite

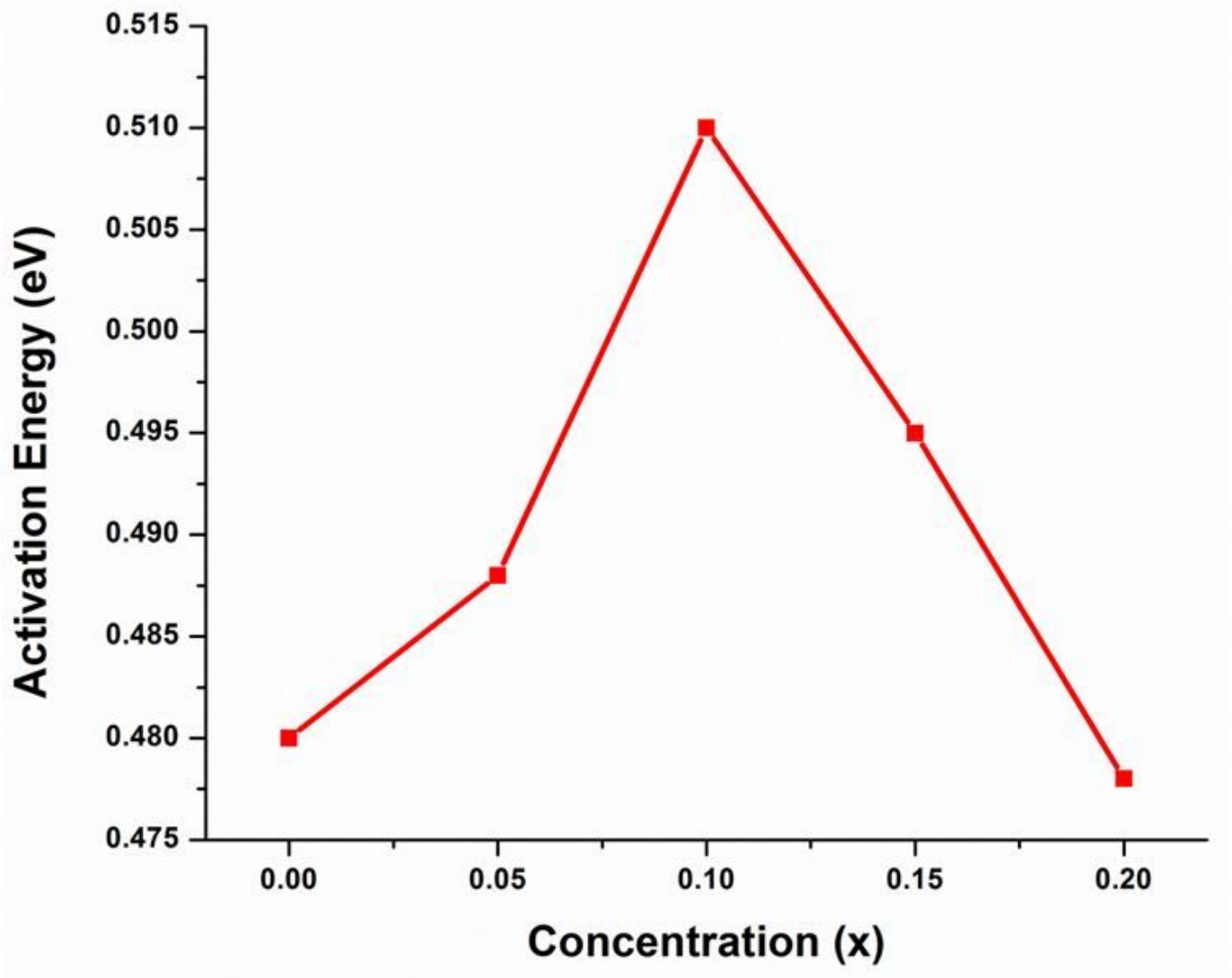


Figure 8

Activation energies of the Co substituted NiCuZn ferrite